Water-Rock Interactions, Ore Deposits, and Environmental Geochemistry: A Tribute to David A. Crerar
© The Geochemical Society, Special Publication No. 7, 2002
Editors: Roland Hellmann and Scott A. Wood

Linking molecular-scale barite precipitation mechanisms with macroscopic crystal growth rates

DIRK BOSBACH[1]

Institut für Mineralogie, Westfälische Wilhelms-Universität Münster, Corrensstr. 24, 48149 Münster, Germany
[1]Current address: Forschungszentrum Karlsruhe, Institut für Nukleare Entsorgung, Postfach 3640
76021 Karlsruhe, Germany
email: bosbach@ine.fzk.de

Abstract—Barite growth in aqueous solution at room temperature was observed in-situ using Atomic Force Microscopy. Various molecular scale growth mechanisms were identified on {001} and {210} cleavage surfaces. The advancement of monolayer steps depends on the crystallographic orientation and increases linearly with the degree of supersaturation. The formation rate of two-dimensional nuclei increases exponentially with increasing supersaturation. The interfacial energy was determined from two-dimensional nucleation data to be 105 mJ/m^2 for the {001} surface and 76 mJ/m^2 for the {210} surface. The critical radius for two-dimensional nuclei in a supersaturation range of $10 < S < 70$ varies between 3–6 Å ($S = [Ba^{2+}][SO_4^{2-}]/K_{sp}$; $[Ba^{2+}]$, $[SO_4^{2-}]$: Ba^{2+} and SO_4^{2-} activities in solution; K_{sp}: solubility product). Up to 10^{13} growth spirals/m^2 have been observed. Their lateral spreading rate and the interstep spacing were determined at various degrees of supersaturation. An overall growth rate was determined at various degrees of supersaturation (up to $S = 50$) by combining the intrinsic $BaSO_4$ attachment rate for the observed microscopic growth mechanisms and the associated reactive surface area. The reactive surface area for these growth mechanisms is not a constant parameter but increases nonlinearly with increasing supersaturation. The macroscopic growth rate as determined from mixed-flow reactor experiments follows a second order rate law, $R = k\times(S\text{-}1)^2$ up to a supersaturation of $S = 50$, with a reaction rate constant of $k = 1.5\times10^{-11} \pm 0.2\times10^{-11}$ mol/m^2 s. An activation energy of 35±8 kJ/mol indicates a surface reaction-controlled growth process. Comparing the macroscopically-determined growth rates with microscopic AFM observations allowed an estimation of the contribution of individual growth mechanisms. Above a supersaturation of $S > 40$-50 two-dimensional nucleation contributes more than 50% to the macroscopic growth rate.

1. INTRODUCTION

Understanding and modeling geochemical processes in low-temperature aqueous environments and hydrothermal systems of the earth's crust requires a detailed knowledge of mineral/water interfacial reactions and the reactivity of mineral surfaces (Hochella, 1990). Sorption processes at mineral surfaces control the distribution and mobility of elements via various uptake and release mechanisms (e.g., Brown et al., 1995). Among these mechanisms, mineral precipitation from aqueous fluids is an important sink for a number of major elements as well as toxic heavy metals. The impact of such a complex process on natural systems can be modeled quantitatively with respect to, for example, the mobility of trace elements using reactive transport computer codes (Lichtner et al., 1996). Ignoring chemical reaction rates can lead to incorrect predictions of chemical mass transfer in sedimentary and metamorphic systems (Cathles, 1983; Steefel & Lasaga, 1992; Lefèvre et al., 1993). Since such codes rely heavily on kinetic data for heterogeneous reactions, reliable data on mineral precipitation rates are needed (Johnson et al., 1998) in order to describe the mobility of aqueous fluids and dissolved species in chemically reactive porous rocks.

Such kinetic data as a function of the chemical affinity can be obtained from macroscopic growth experiments in batch reactor or mixed-flow reactor systems (Zhang & Nancollas, 1990). Rate laws obtained from such experiments have been used to identify rate controlling mineral precipitation mechanisms, such as spiral growth or two-dimensional (heterogeneous) nucleation in solutions (Nielsen, 1984; Brady & House, 1996). However, mineral growth is a very complex process with several independent molecular scale mechanisms on various crystallographic surfaces, with each surface having a unique atomic bonding environment contributing to the macroscopic growth rate (Lasaga, 1995). With a changing degree of supersaturation the contribution of individual mechanisms on certain surfaces to the macroscopic growth rate can change (Sunagawa, 1987). The morphology and texture of the precipitated mineral reflects this behavior macroscopically (Rimstidt, 1997).

The aim of this paper is the identification of molecular-scale precipitation mechanisms under various degrees of supersaturation using Atomic Force Microscopy (AFM). In addition, the reactive surface area with respect to a particular mechanism under a certain degree of supersaturation has been determined. Combining macroscopic mineral growth ex-

periments and AFM observations allows an estimation of the contribution of various microscopic growth mechanisms to the total reaction rate. Precipitation of barite, $BaSO_4$, and isostructural celestite, $SrSO_4$, are used as a model system. Relatively pure barite precipitates are frequently found as a gangue mineral formed under hydrothermal conditions (Rimstidt, 1997); barite precipitates are also the major Ba sink in marine environments (Paytan et al., 1996). Furthermore, barite scale formation during secondary oil recovery is a costly problem (Benton et al., 1993). Barite precipitates over a broad supersaturation range due to temperature or pressure drops, or due to mixing of two fluid reservoirs. For example, during secondary oil recovery, ocean water with 28.1 mmol/L SO_4^{2-} (Stumm & Morgan, 1995) mixes with formation waters containing Ba^{2+} at concentrations up to 18.2 mmol/L (Hardy & Simm, 1996), thereby producing high degrees of supersaturation (dependent on mixing proprotions) with respect to the barite equilibrium solubility concentration of 0.01 mmol/L .

2. EXPERIMENTAL METHODS

Crystal growth was observed in-situ on a molecular level using a Digital Instruments NanoScope III MultiMode AFM operating in contact mode at room temperature with a commercially available fluid cell. Si_3N_4 cantilevers with a length of 100 µm with integrated pyramidal TwinTip™ tips were used (spring constant: 0.6 N/m). The maximum scan rate used in this study was about 15 scan line/s. Therefore, it took about 17 s to aquire an AFM image consisting of 256 x 256 data points. The observable reaction rate is in the range of 10^{-6} - 10^{-10} mol/m^2 s (Dove & Platt, 1996). Freshly cleaved, optically clear, natural barite crystals from various locations were mounted in a cup-like Teflon sample holder (as part of the AFM fluid cell) with a carbon-based adhesive (Leit-C, Plano). The crystallographic orientation of the sample crystal with respect to the AFM scan direction was determined after the growth experiment by X-ray defraction using an Enraf-Nonius precession camera with the Mo Kα line (40 kV, 30 mA). Before running the actual growth experiment, the sample was initially exposed to deionized water in order to dissolve and clean the topmost mineral surface layer, thus reducing the risk of surface contamination which could affect the growth experiments.

Due to strong interactions between the AFM tip and the sample surface, with a loading force in the nanonewton range, it has been shown that under certain circumstances the dissolution rate of molecular steps on a calcite cleavage surface can be mechanically enhanced (Park et al., 1996). Although contact mode AFM potentially affects the observed precipitation processes, it allows fast scan rates, which is crucial for imaging rapid precipitation mechanisms such as two-dimensional nucleation. In addition, the faster the inherent surface reaction, the smaller the relative effect the AFM tip potentially has on the observed kinetics. Comparing the microtopography of surface areas which were imaged over a period of time with surface areas that were imaged only once at the end of an experiment allows a determination of whether the observed crystal growth processes were obstructed by the AFM tip.

Step velocities of advancing monolayer steps were determined from flow-through experiments with a constant flow rate of up to 10 µL/s. Measured step velocities were independent of the flow rate, indicating that the growth rate was not transport controlled. In contrast, two-dimensional nucleation experiments in the AFM fluid cell were done in free drift experiments where a supersaturated solution was injected into the AFM fluid cell. At high degrees of supersaturation the nucleation rate was too high to be observable with AFM. Steady-state nucleation rates could not be obtained with a flow-through setup. Therefore, during the actual growth experiments the fluid flow was stopped after injection of the fluid into the AFM fluid cell. As a consequence, the fluid composition changed with time.

Supersaturated $BaSO_4$ and $SrSO_4$ were prepared by mixing equimolar Na_2SO_4 and $Ba(NO_3)_2$/$Sr(NO_3)_2$ solutions made of analytical grade chemicals and deionized water immediately before the experiment. The degree of supersaturation was determined using the aqueous speciation code in PHREEQC (Parkhurst, 1995). In this study, the supersaturation is expressed as $S = IAP/K_{sp}$, where IAP is the ion activity product of the ionic species in solution and K_{sp} is the solubility product (log K_{sp}(barite) = -9.96 (Blount, 1977) and log K_{sp}(celestite) = -6.62: Reardon & Armstrong, 1987). Macroscopic barite growth experiments were done in a mixed-flow reactor. Steady-state growth rates were obtained after initially elevated reaction rates.

Barite has an orthorhombic structure (space group: Pmna, a = 8.87 Å, b = 5.45 Å, c = 7.14 Å, Colville, 1967). Each unit cell consists of two $BaSO_4$ layers parallel to {001}, which are symmetrically related to each other via a 2_1 diad axis perpendicular to {001} (Fig. 1a). Good cleavage occurs parallel to {001} and {210} (Deer et al., 1992) (Fig. 1b). A natural hydrothermally-formed barite sample from Bad Lauterberg (Germany) was ground and a grain size fraction between 65 – 200 µm was separated in various stages. The smallest particles were removed by washing with water. Impurities were removed with an isodynamic magnetic separator and heavy liquid separation. ICP

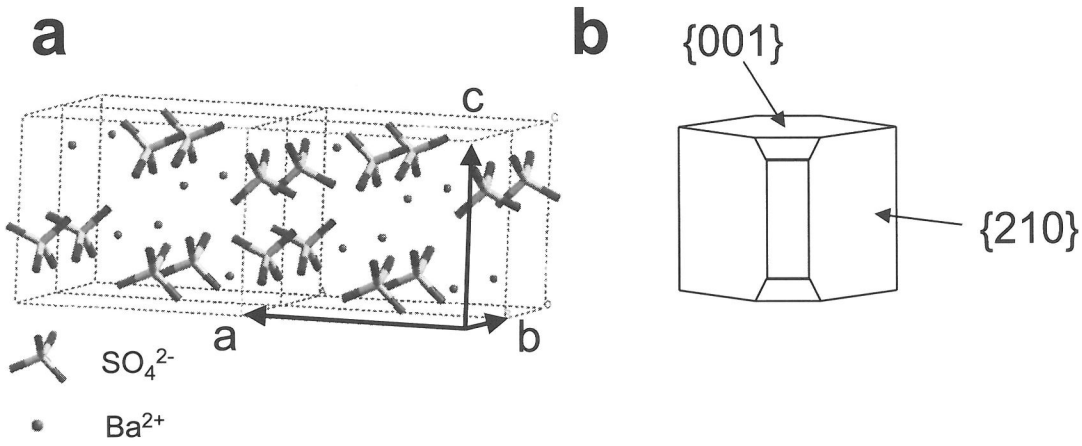

Figure 1: a) Barite has an orthorhombic crystal structure (space group: Pnma). b) The dominant crystal faces of naturally occurring barite crystals are parallel to {001} and {210}. They are energetically the most stable barite crystal faces, based on periodic bond chain theory (Hartman & Strom, 1989).

analysis showed no significant contamination by Sr or other trace elements. Only a very small amount of intergrown quartz could not be removed.

In order to derive a surface area normalized-growth rate, the initial specific surface area of barite was determined to be 0.5 m^2/g, using N_2 and the BET method (Haul & Dümbgen, 1960). The sample was heated to 300 °C prior to N_2 adsorption. However, scanning electron microscope images showed that the surfaces of the barite particles were irregular. Therefore, crystal growth rates were initially elevated with respect to euhedral crystals. The fluid composition during the experiment was monitored via solution conductivity measurements, using a 4-electrode open-geometry conductivity cell (WTW TetraCon 96). The experiments were done in a Teflon mixed flow reactor with a suspended stirring bar in order to exclude grinding effects during the experiment. The observed barite growth rate was independent of the stirring rate, thus excluding a diffusion-controlled reaction. A typical reactor experiment ran for about 24 hours with a fluid volume of 150 mL and 200 mg of barite. Depending on the degree of supersaturation, steady state was reached after 1-5 hours.

3. MOLECULAR-SCALE PRECIPITATION MECHANISMS

Mineral growth from aqueous solution is a complex process which involves several independent microscopic mechanisms. Growth units (ions or molecules) are transported by diffusion or convection to the mineral/fluid interface, where they adsorb to the mineral surface and partially dehydrate. Adsorbed species might move along the surface via surface diffusion. Eventually, they become integrated into the crystal lattice upon complete dehydration. The most likely surface site for the integration step is a kink-site along a monolayer step. As a consequence, monolayer steps advance parallel to the mineral surface. They represent the most reactive parts of a mineral surface exposed to a supersaturated solution.

3.1. Two-dimensional Island Morphology and Molecular Step Growth

In a supersaturated solution growth units tend to form islands on a mineral surface, which grow laterally with a distinct step velocity that depends on both the supersaturation in the aqueous fluid and the crystallographic orientation. As a consequence of this the islands develop a distinct morphology. In supersaturated solutions, islands with a height of one $BaSO_4$ layer form on barite {001} and {210} surfaces (Fig. 2). On the {001} surface, islands develop a circular sector shape, which is defined by molecular step edges parallel to <120> and a curved step edge (Fig. 3a) (Bosbach et al., 1998; Pina et al., 1998a, b). The curvature can be described in terms of the island diameter parallel to <120> and to [100]. For a perfectly circular

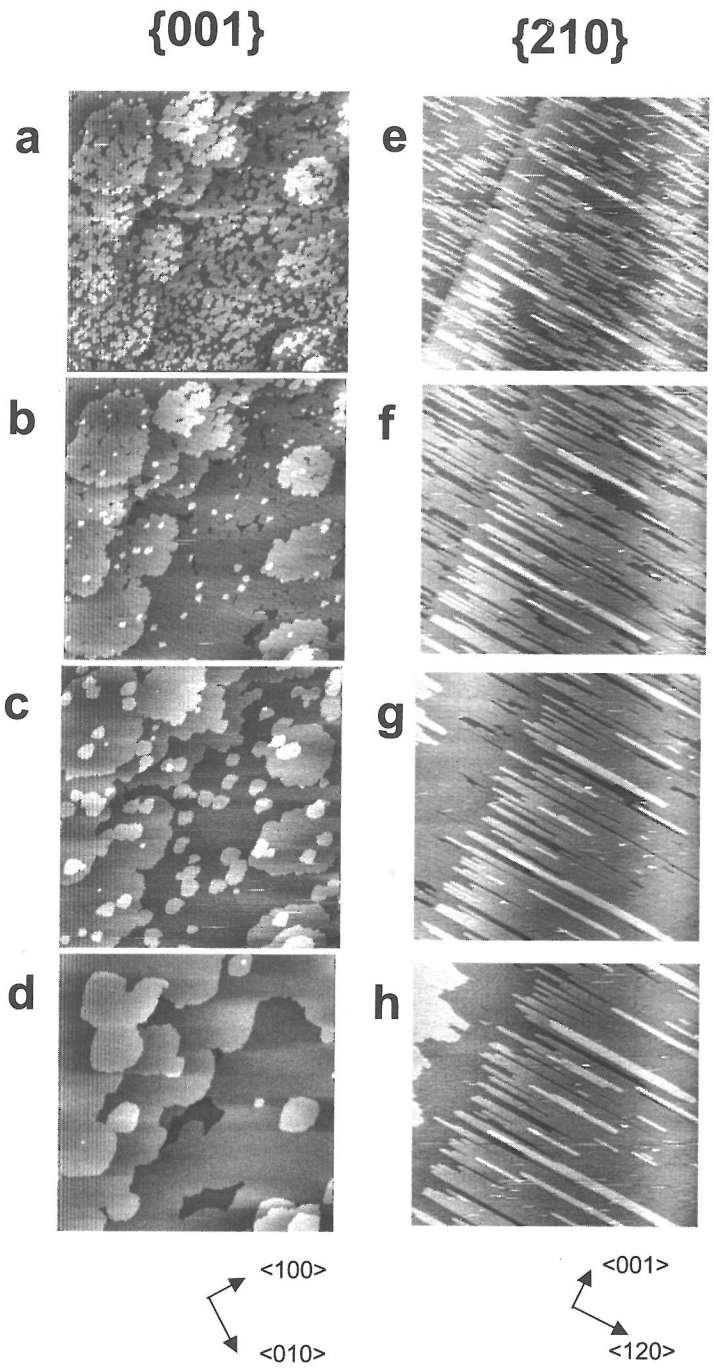

Figure 2: Growth sequences on the barite {001} (a-d) and {210} (e-h) surface. All images were taken in contact mode, in situ, under free-drift conditions. a) The initial supersaturation was $S = 70$ (scan size 1.8 x 1.8 µm, scan rate: 15 Hz, 256 x 256 pixel). The island height of 3.5 Å represents one $BaSO_4$ layer. b)-d) After the formation of two-dimensional islands monolayer step growth is the dominant growth mechanism. e) The initial supersaturation was $S = 41$ (scan size 6.0 x 6.0 µm, scan rate: 10.2 Hz, 256 x 256 pixel). f)-h) The lateral spreading due to monolayer step growth is highly anisotropic, resulting in an elongated, needle-like morphology. The island height also represents one $BaSO_4$ layer.

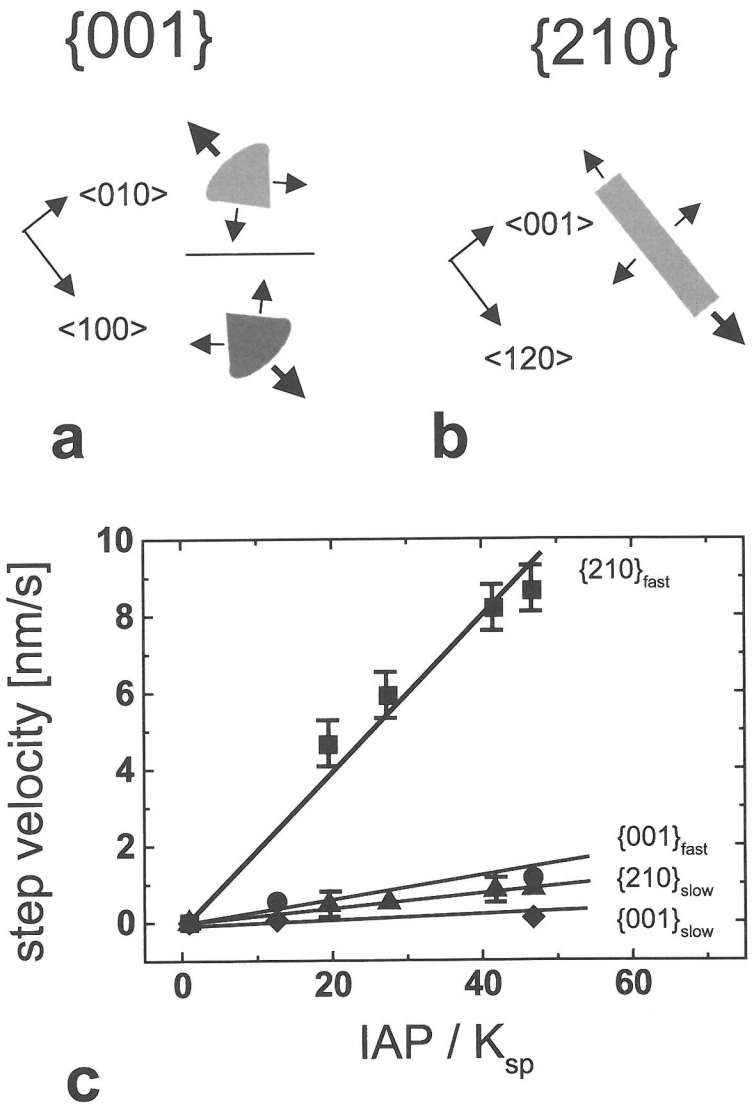

Figure 3: a) Islands on the {001} surface with a height of one $BaSO_4$ layer have a sector shape morphology, with step edges parallel to <120> and a curved step edge. In alternating layers at c = 0 and c = 0.5 islands point in the opposite direction as a consequence of a 2_1 diad axis perpendicular to the {001} surface. The curved step edges grow significantly faster than the step edges parallel to <120>, as indicated by arrows. b) On the {210} surface molecular islands have an elongated needle-like morphology, with step edges parallel to <001> and <120>. One of the short step edges parallel to <001> advances significantly faster compared to the monolayer step parallel to <001> growing in the opposite direction. Molecular steps parallel to <120> grow with a similar rate. c) The growth rate of molecular steps increases linearly with supersaturation. Anisotropic monolayer step growth can be observed on the {001} as well as on the {210} surface.

curved step edge the ratio would be 1. However, on the barite {001} surface the ratio of <120> diameter/[100] diameter is consistently about 1.1 for islands with an average diameter between 100 and 1500 nm. The stability of steps parallel to <120> can be explained by periodic bond chain (PBC) theory (Hartman, 1987). Strong bonds parallel to <120> relative to bonds perpendicular to these directions result in a low kink den-

sity along these steps. Monte-Carlo calculations on the basis of attachment energies for various sites on a barite {001} surface and the resulting double kink site formation probabilities can explain the curved step edge (Pina et al., 1998a). The deviation from the perfectly circular sector morphology is also a consequence of this selective attachment of growth units. Steps grow anisotropically, with the curved step edges advancing about 10 times faster than the steps parallel to <120> (Fig 3a). In alternating $BaSO_4$ layers the orientation of the sector is reversed due to the 2_1 diad axis perpendicular to the {001} surface (Bosbach et al., 1998; Pina et al., 1998a). If a fast growing step edge joins a slow growing step in the underlying $BaSO_4$ layer, the step velocity of the slow step controls the advancement of the resulting double step. Thus, a complex interaction between step growth kinetics and microtopography occurs.

The growth of islands on the {210} surface is different compared to the {001} surface (Pina et al., 1998b). Islands grow as long needles with a height of 3.4 Å, this representing one $BaSO_4$ layer (Fig. 2e-h). The elongated morphology is again a consequence of an anisotropic monolayer step growth (Fig. 3c). Along the long axis of the needles parallel to <001>, step growth is significantly faster in one direction relative to the opposite direction (Fig. 3b). The fastest growth direction is not reversed in alternating $BaSO_4$ layers on the {210} surface. Step growth of steps parallel to <120> is comparable to the slow growing steps parallel to <001>.

Monolayer step growth increases linearly with supersaturation for monolayer steps observed on the {001} surface, as well as on the {210} surface (Fig. 3c). In general, step edges are more reactive with respect to molecular step growth on the {210} surface relative to the {001} surface. In order to link molecular step growth with the macroscopic growth rate it is critical to estimate the rate at which new steps are generated.

3.2. Two-dimensional Nucleation Kinetics

The formation rate and the dimensions of two-dimensional nuclei strongly depend on the interfacial energy, σ, between the mineral surface and the adjacent fluid, as well as on the degree of supersaturation. Energetically, this process can be discussed in terms of the change in Gibbs free energy of formation of two-dimensional nuclei, ΔG:

$$\Delta G = n \cdot k \cdot T \cdot \ln(S) + \sigma \cdot 2 \cdot \pi \cdot r \cdot h \qquad (1)$$

In the first term of Eqn. 1, n represents the number of growth units ($BaSO_4$) in the island, k is the Boltzmann constant, and T the temperature in K. It will be assumed that one growth unit for barite growth consists of ($BaSO_4$), which represents a quarter of the unit cell. In the second term of Eqn. (1), r is the radius and h the height of a pancake-like island. Clearly, the formation of nuclei is energetically not favored at low degrees of supersaturation. Only above a certain size are nuclei stable and able to grow laterally. Above this critical size islands are called nuclei, whereas below this they are called embryos (Chernov, 1984). Due to the energy barrier for forming stable nuclei, their formation is thought to be an efficient growth mechanism only at high degrees of supersaturation. The critical size of nuclei is supersaturation-dependent. Although a theoretical framework has been developed for describing the thermodynamics of two-dimensional nucleation in aqueous solution (Nielsen, 1964; Walton, 1965; Hillig, 1966), it is still not well understood. In many cases, the interfacial energy and the critical dimensions of such nuclei are not known. Unfortunately, these processes are not accessible directly with light microscopic techniques, such as differential interference contrast microscopy (DICM). Despite their excellent vertical resolution, which allows for the imaging of molecular scale steps, the lateral resolution is limited by the wavelength of the light source. Nevertheless, these methods have provided detailed in-situ information on spiral growth and step growth in aqueous fluids (Sunagawa, 1987).

Figure 2 shows growth sequences on barite {001} and {210} cleavage surfaces. At the beginning of a growth experiment in the AFM fluid cell, 2 mL of a supersaturated solution was injected in less than one second, thus ensuring that the entire volume of the fluid cell of about 100 µl had been replaced by the supersaturated solution. After a short induction time, two-dimensional islands formed on atomically flat terraces (Fig 2). On the {001} surface (Fig. 2a-d), upon formation of the first layer, the islands spread laterally and subsequently only a few new islands form. Since the fluid flow was stopped after the initial injection of the supersaturated solution, the fluid composition became depleted in Ba^{2+} and SO_4^{2-}, which resulted in a reduced degree of supersaturation and consequently in a reduced growth rate. Due to the fast reaction rate relative to the scan speed of the AFM, the formation of islands could not be observed when constantly feeding the fluid cell with supersaturated solution. Although this would ensure constant composition conditions, the experiments were performed under free drift conditions. Therefore, steady-state nucleation rates could not be extracted.

During the period of initially high degree of supersaturation, the lateral spreading of the islands is fast relative to the scan speed of the AFM, and it is there-

fore difficult to follow microtopographic changes (Figs. 2 a and e). After injection of the supersaturated solution, the first image (Fig. 2a) was generated (from bottom to top), requiring about 17 sec for the complete image. At the bottom of the image (Fig. 2a), individual islands can be clearly distinguished. Upon formation, these islands grow laterally via step growth. Therefore, in the top region of the image (Fig. 2a), individual islands can no longer be distinguished because they have spread laterally and cover almost the entire crystal surface. Furthermore, a few islands have formed on top of the first islands (Fig. 2b), but at a lower density, as a consequence of depletion of the $BaSO_4$ solution. Repeating such experiments with various initial supersaturations reveals that the initial island density increases exponentially with increasing supersaturation (Fig. 4a), as one would expect according to the theoretical work by Nielsen (1964), Walton (1965) and Hillig (1966), which predicts an exponential increase of the steady state nucleation rate, J, with increasing supersaturation:

$$J = J_0 \times \exp\left(-\frac{\pi \times h \times \omega \times \sigma^2}{(R \times T)^2 \times \ln S}\right) \qquad (2)$$

where ω represents the molecular volume. Eqn. (2) also assumes that the two-dimensional nuclei have pancake-like morphology with height h. The pre-exponential factor J_0 is related to the efficiency of ion collisions with the mineral surface.

The island density, which was estimated after injecting a supersaturated solution into the AFM fluid cell (Figs. 2a and 2e) can be referred to as an initial surface nuclei density, N_i. In the case of three-dimensional nucleation it has been shown that such an initial nucleation rate is directly proportional to the nucleation rate under steady state conditions (Nielsen, 1964; Lasaga 1998). A linear correlation between $ln\ N_i$ vs. $(ln\ S)^{-2}$ for the case of three-dimensional nucleation has been interpreted as an indication that the above given thermodynamic approach applies to the precipitation of barite and isostructural crystals (Nielsen, 1964). Similarly, in the case of the two-dimensional nucleation data presented here, $ln\ N_i$ for barite and celestite can be plotted versus $(ln\ S)^{-1}$, yielding a good linear correlation (Fig. 4b). The interfacial energy for the mineral/fluid interface can be determined from the slope of the linear fits in Fig. 4b based on equation (2). In case of barite one obtains 105 mJ/m^2 from the observations on the {001} and 76 mJ/m^2 on the {210} surfaces. However, these values do not represent the interfacial enrergies of the {001} and {210} surface, but rather they are related to the edge surfaces of the nuclei. Recently, He et al. (1995) found a value of 93.4 mJ/m^2

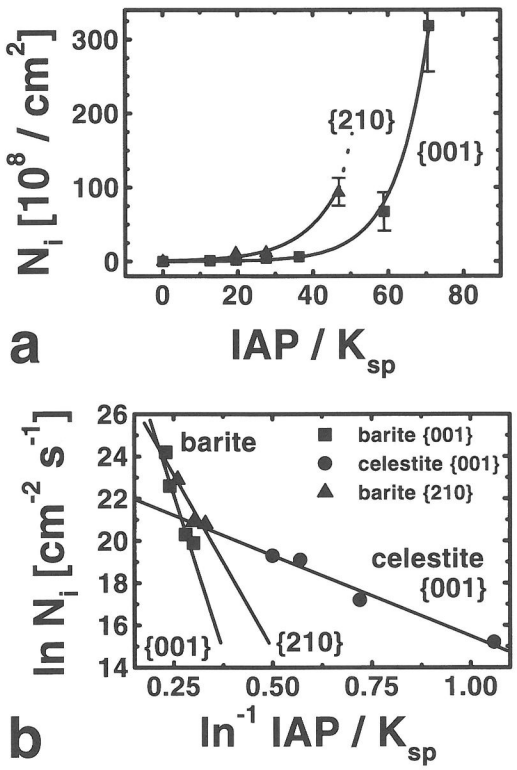

Figure 4: a) The observed initial density of islands, N_i, after injecting a supersaturated solution into the AFM fluid cell increases exponentially on the {001} and {210} barite surfaces. b) A linear correlation between $ln\ N_i$ versus $(ln\ IAP/K_{sp})^{-1}$ for the barite {001} and {210} surfaces, as well as for the celestite {001} surface, suggest that the observed island density can be related to a steady-state nucleation rate.

for barite from macroscopic three-dimensional (homogeneous) nucleation experiments at low ionic strength at room temperature. However, the macroscopically determined value integrates over several crystal surfaces with various crystallographic orientations and interfacial energies. Based on PBC theory (Hartman, 1987), the crystal morphology for a barite crystal grown at low to moderately high degrees of supersaturation has been predicted to be defined by a combination of {001} and {210} crystal faces. Furthermore, a statistical evaluation of the crystal morphology of naturally occuring barite crystals showed that {001} and {210} are the most dominant crystal faces (Hartman & Strom, 1989). Therefore, the interfacial energy derived from macroscopic three-dimensional nucleation experiments should be equal to the weighted sum of the interfacial energies obtained on the {001} and {210} surfaces. For celestite one ob-

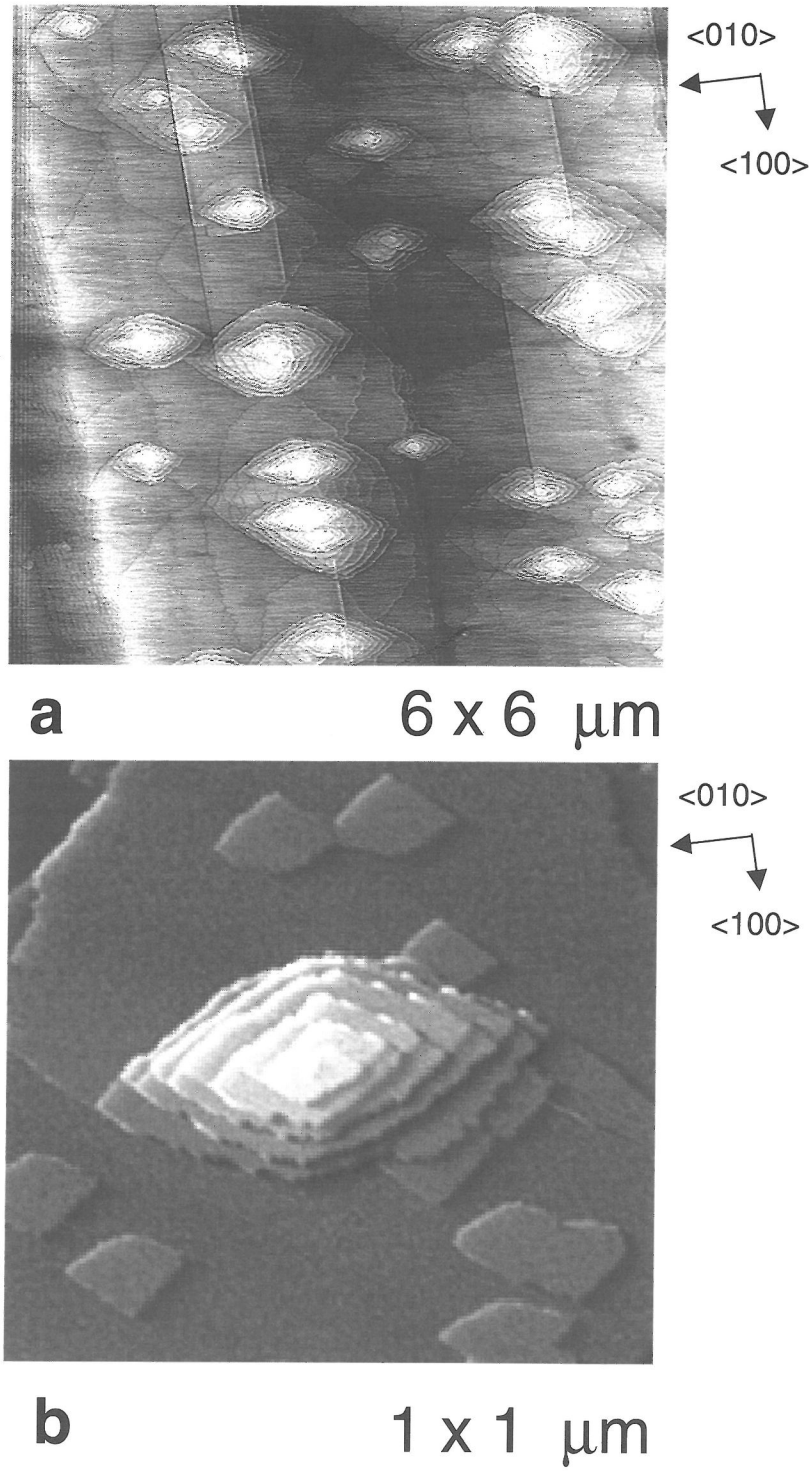

Figure 5: On the barite {001} surface growth spirals develop in the vicinity of dislocation cores in supersaturated solutions. a) The image was taken 30 min after exposure of a freshly cleaved sample to a supersaturated solution with $S = 25$. The spiral density varies between (0 to 10^{13} m^{-2} on the same crystal. b) Due to the growth anisotropy in alternating $BaSO_4$ layers, the shape and the lateral spreading of the growth spirals are controlled by the slowest growing molecular steps. Each spiral consists of monolayer and double layer steps. (after Pina et al., 1998a)

tains 38 mJ/m^2 for the interfacial energy from AFM observations on the {001} surface. This value is significantly smaller than the 105 mJ/m^2 obtained for the barite {001} surface, as one would expect following the empirical relation by Nielsen & Söhnel (1979), which relates the solubility to the interfacial energy.

In addition to the kinetic aspects of nuclei formation, the critical size of nuclei is another important parameter for understanding two-dimensional nucleation. Assuming a pancake-like morphology, the number of growth units, n_{crit}, in a nucleus with critical size is given by (Lasaga, 1998):

$$n_{crit} = \frac{\omega \cdot \sigma^2 \cdot h \cdot \pi}{(k \cdot T \cdot \ln S)^2} \quad (3)$$

In the supersaturation range of $10 < S < 70$ the number of growth units in a nucleus with critical size varies between 7-5 on the barite {001} surface and between 6–4 on the {210} surface. Assuming a pancake-like morphology with a height of one $BaSO_4$ layer, the corresponding critical radius varies between 6 and 3 Å on the {001} surface and 5–2 Å on the {210} surface. These values agree well with the predicted critical size of nuclei by Nielsen (1964), who estimated that two dimensional nuclei forming at a mineral/fluid interface consist of 10 or fewer ions.

3.3. Spiral Growth

Due to the interfacial energy that is involved in the formation of two-dimensional nuclei, this mechanism is the predominant growth mechanism only at high degrees of supersaturation. Following Eqn. (2), at near-equilibrium conditions the critical radius for nuclei would be large (e.g., for barite {001} 150 Å at S = 5) and the probability for their formation is small. However, screw dislocations intersecting a mineral surface provide a continous source of monolayer steps. The subsequent attachment of growth units to these steps result in the development of growth spirals (BCF model, Burton et al., 1951).

The development of growth spirals on the barite {001} surface was monitored over several hours (Fig. 5). As a consequence of the monolayer step growth anisotropy, fast growing monolayer step edges parallel to <120> catch up with underlying slow growing monolayer step edges and form a two-layer step. The lateral spreading of growth spirals is controlled by such two-layer step edges parallel to <120>. The lateral spreading of the growth spirals agrees within the limits of error with the slowest step velocity observed for monolayer steps parallel to <120>. The morphology of growth spirals should be defined by steps parallel to these directions. However, this is only the case for small growth spirals and the 3–4 topmost $BaSO_4$ double layers of larger spirals (Fig. 5b). At the bottom of a spiral, double steps are curved and not strictly aligned parallel to <120>. The curvature can be explained by the preferential attachment kinetics of growth units and the resulting probability for the formation of double kink sites at certain sites along these steps (Pina et al., 1998a). The curvature of the <120> double layer steps can only be found within growth spirals. On the contrary, for large islands with a height of a single $BaSO_4$ layer, steps with the slowest growth rate have crystallographically aligned steps parallel to <120> , independent of the size.

While a growth spiral develops on a freshly cleaved barite surface, its growth rate (in mol/L) at a given degree of supersaturation is not a constant but increases as it becomes larger because it generates new molecular steps. A rough estimation based on the dimensions of single spirals shows that a typical growth spiral that has developed within one hour at a supersaturation of S=10 has a growth rate of about 10^{-21} mol/s. In order to determine a macroscopic surface area-normalized steady-state growth rate from microscopic experiments under non-steady-state conditions, one has to determine the dislocation density. Unfortunately, the defect density is not always homogeneously distributed over the entire barite surface (Bosbach et al., 1998). On {001} cleavage surfaces the observed dislocation density was up to 10^{13} m^{-2}. Assuming this defect density, one can calculate a macroscopic growth rate of about 10^{-8} mol/m^2 s, based on the observed growth rate of individual spirals within one hour under non-steady state conditions. However, under steady-state conditions, where the entire barite surface is covered by monolayer or two-layer steps, the macroscopic growth rate is controlled by the step spacing or step density and the step growth.

In contrast to the {001} surface, the formation of growth spirals was never observed on the {210} surface, even after several hours of exposure to a supersaturated solution. However, dislocations with a Burgers vector equivalent to one $BaSO_4$ layer parallel to {210} could be identified. Spiral growth on the {210} surface seems to be a structurally self-inhibited mechanism as a consequence of a strong anisotropy for the growth of molecular steps. Consequently, the contribution of spiral growth on the {210} surface is negligible for growth at room temperature and for supersaturations of $S \leq 20$.

Based on in-situ observations with AFM, molecular scale barite growth mechanisms can be identified at various degrees of supersaturation. However, in order to evaluate the importance of these observed growth mechanisms with respect to the macroscopic crystal growth rate, surface area-normalized reaction

rates have to be determined at various degrees of supersaturation as a reference.

4. MACROSCOPIC BARITE GROWTH RATES

At a macroscopic scale, barite growth in dilute aqueous solutions at an ionic strength of 10^{-4} M follows a second order growth rate law according to:

$$R = k \cdot (S-1)^2 \quad (4)$$

within the investigated supersaturation range (up to S=50) with a rate constant of $1.5\times10^{-11} \pm 0.2\times10^{-11}$ mol/m^2 s (Fig. 6). The growth rate varies between about 10^{-11} mol/m^2 s under near equilibrium conditions to 1.2×10^{-8} mol/m^2 s at S = 50. The activation energy for barite growth in a supersaturation range of $8 < S < 26$ was determined from simple batch reactor experiments at various temperatures from 21-50 °C to be 35±8 kJ/mol, following an Arrhenius approach.

A 2nd order rate law has been interpreted as an indication that the direct integration of growth units into the crystal lattice at molecular steps associated with growth spirals is the rate controlling step (Zhang & Nancollas, 1990; Brady & House, 1996). Below a threshold supersaturation where two-dimensional nucleation becomes the rate-controlling mechanism, spiral growth according to the BCF model should be the dominant precipitation mechanism under near equilibrium conditions (Burton et al., 1951; Nielsen, 1984). A rate law with a reaction order greater than 2 has been interpreted as an indication that two-dimensional nucleation is the dominant mechanism, which is known as the birth & spread model (O'Hara & Reid, 1973). The 2nd order rate law observed for barite suggests, therefore, that spiral growth is the dominant growth mechanism within the investigated supersaturation range, up to S = 50. Furthermore, similar macroscopic experiments by Doremus (1958) and by Liu et al. (1976) show a 2nd-order rate law up to S = 230.

5. LINKING MICROSCOPIC MECHANISMS AND MACROSCOPIC PRECIPITATION RATES

Relating the observed molecular-scale barite growth mechanism to the macroscopic rate law can be achieved by estimating the contribution of: (i) step growth of cleavage steps, (ii) spiral growth, and (iii) two-dimensional nucleation on every crystal face. Linking molecular-scale growth mechanisms and macroscopic reaction rates ultimately requires that the reactive surface area be determinable. This has recently been demonstrated for the case of dissolution of structurally highly anisotropic sheetsilicates (Rufe & Hochella, 1999; Bosbach et al., 2000). Reactive surface area is not a constant parameter but depends on the monolayer step density in the case of step growth, the dislocation density in the case of spiral growth under non-steady state conditions, on the nucleation rate in the case of two dimensional nucleation, and on the lateral step velocity. In addition, the step density associated with growth spirals growing under steady state conditions depends on the degree of supersaturation.

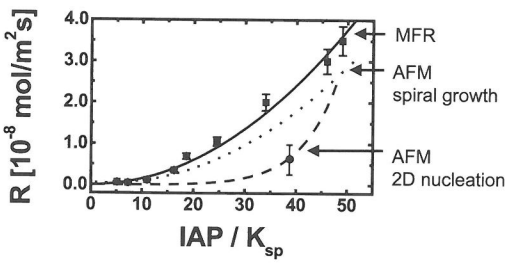

Figure 6: The macroscopic barite steady-state growth rate as determined from mixed flow reactor (MFR) experiments follows a second order rate law (solid line). A macroscopic growth was calculated on the basis of the island density (two dimensional nucleation) and the monolayer step growth data obtained from AFM observations (dashed line). An error bar at a selected degree of supersaturation indicates the uncertainty based on the errors for the individual measurements for step growth and two-dimensional nucleation. The contribution of spiral growth (dotted line) has been predicted based on AFM observations at low degrees of supersaturation up to S = 20. Above a supersaturation range of $40 < S < 50$ growth associated with two-dimensional nucleation becomes the predominant precipitation mechanism.

5.1. Monolayer Step Growth

In the case of monolayer step growth only a small fraction of the entire mineral surface is reactive with respect to this mechanism. If one considers only the mineral surface adjacent to monolayer steps as the reactive part of the mineral surface for the attachment of one growth unit, one can estimate a macroscopic growth rate on the basis of measured step velocities (Fig. 3c) and observed step densities. Freshly cleaved barite {001} surfaces have a reactive surface area that represents up to 0.1% of the total surface area. Since the cleavage process is not well defined, the values scatter significantly and the value of 0.1% represents the highest observed monolayer step density. Under near equilibrium conditions at S = 2 the reactive surface area-normalized growth rate can be estimated to be about 10^{-9} mol/m^2 s. Therefore, the growth rate normalized to the total surface area should be about 10^{-12} mol/m^2 s. The macroscopically-determined

total (BET) surface area normalized-growth rate under this condition is about 10^{-11} mol/m^2 s. The barite particles used for the macroscopic growth experiments were not as flat as the cleavage surfaces used for the AFM experiments. Although the intrinsic $BaSO_4$ attachment rate was comparable in the macroscopic and microscopic (AFM) experiments, the macroscopically-determined growth rate is faster than the growth rate obtained from AFM observations. However, comparing these rates allows an estimation of the reactive surface area of the material used in macroscopic experiments.

5.2. Spiral Growth

The development of growth spirals on freshly cleaved barite surfaces increases the reactive surface area significantly, although the total surface area as determined from BET measurements would only increase slightly. However, under steady-state conditions, growth spirals on a crystal surface cover the entire crystal surface and the microtopography of the crystal surface would establish a constant step density with a constant reactive surface area/total surface area ratio, which only depends on the degree of supersaturation. The BCF model (Burton et al., 1951) predicts, and AFM observations confirm, that the step density associated with growth spirals increases with increasing supersaturation. Therefore, the number of reactive sites along step edges depends on the degree of saturation and cannot be considered as a constant.

The growth rate of spirals normal to the surface can be used to estimate the steady-state normal growth of a crystal. At a supersaturation of $S = 10$ the height of growth spirals on the barite {001} surface increases at about 5×10^{-4} nm/s. A macroscopic growth rate can be estimated to be 5×10^{-9} mol/m^2 s, by assuming an average diameter of 100 μm for cubic particles. The macroscopically-determined growth rate at $S = 10$ is 1.0×10^{-9} mol/m^2 s. Considering the fact that AFM observations suggest that spiral growth does not contribute significantly to the growth of the {210} surface, an estimation for a macroscopic growth rate based on AFM observations on the barite {001} surface agrees very well with the macroscopically observed rate (Fig. 6). Spiral growth normal to the {001} surface was only determined over a narrow supersaturation range, up to $S < 20$.

5.3. Two-dimensional Nucleation

The formation of two-dimensional nuclei and lateral spreading of islands was imaged on the {001} and the {210} surface. The entire barite substrate is covered with islands, which implies that 100% of the crystal surface can be considered to be reactive with respect to nucleation events.

Combining the observed island density (Fig. 4a) and the monolayer step growth rates on the {001} and {210} surfaces (Fig. 3c), one can calculate a macroscopic rate with respect to two-dimensional nucleation (Fig. 6). Depending on the relative size of the {001} and {210} crystal faces, growth associated with two-dimensional nucleation contributes more than 50% to the total growth rate above a threshold supersaturation range of $40 < S < 50$. Assuming that the microscopic in-situ AFM experiments were performed under conditions comparable to the macroscopic mixed-flow reactor experiments, the difference between the macroscopically-obtained growth rate and the predicted growth rate based on AFM observations (of two-dimensional nucleation) is due to spiral growth.

In the case of an ideal system, where the precipitating crystal and the substrate are identical materials, the macroscopic crystal growth rate at high degrees of supersaturation can be predicted on the basis of microscopically-characterized two-dimensional nucleation processes. However, the composition of aqueous fluids in nature can be very complex and the heterogeneous precipitation on a foreign substrate is very common. As a simple example, the precipitation of a solid solution system such as barite growth on a celestite ($SrSO_4$) {001} substrate was imaged in-situ with AFM (Fig. 7). The lattice constants of isostructural celestite (a = 8.38 Å, b = 5.37 Å, c = 6.85 Å) and barite (a = 8.87 Å, b = 5.45 Å, c = 7.14 Å) differ by up to 6%. AFM observations showed no indication for a structural surface reconstruction on the barite {001} surface (Bosbach et al., 1998). Although there is no experimental evidence available, this will also be assumed for celestite. There is a lattice mismatch of 6% parallel to <100>, 2% parallel to <010> , and 3% parallel to <120>. Therefore, epitaxial growth of pure barite or a $(Ba,Sr)SO_4$ solid solution on the celestite substrate are affected by these differences.

Heterogeneous precipitation in the $(Ba,Sr)SO_4$ solid solution aqueous system was observed in situ at various degrees of supersaturation. In these AFM growth experiments, monolayer step edges were generated by etching the celestite {001} surface in deionized water. Shallow triangular etch pits formed within 5 minutes. The morphology of the etch pits is defined by molecular steps parallel to <010> and <120> (Fig. 7), which has also been observed on barite {001} (Putnis et al., 1995; Bosbach et al., 1998; Higgins et al., 1998). The orientation of the etch pits is reversed in alternating $SrSO_4$ layers as a consequence of the 2_1 diad axis perpendicular to

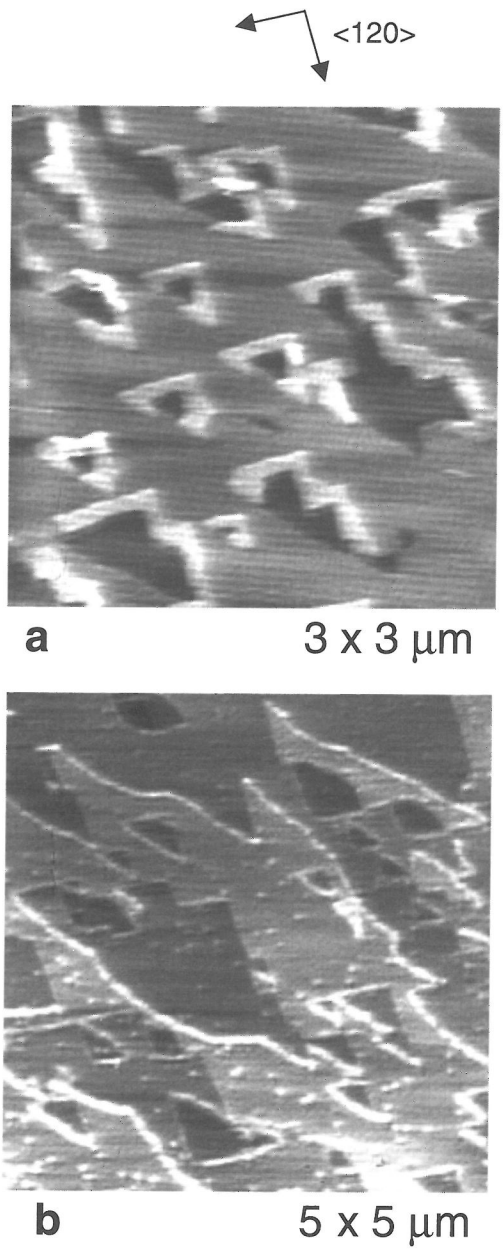

Figure 7: a) Precipitation of $BaSO_4$ (barite) onto an isostructural $SrSO_4$ (celestite) substrate at a supersaturation of $S = 170$ only occurs along monolayer step edges. The celestite (001) substrate was etched in pure water before the supersaturated solution was injected. As a consequence of the etching process, shallow triangular etch pits with a depth of one $SrSO_4$ layer have developed. The triangular shape of the etch pits is defined by molecular step edges parallel to [010] and <120>. $BaSO_4$-rich precipitates nucleate preferentially on step edges parallel to <120>. Flat celestite terraces are not covered with islands. b) At a higher supersaturation of $S = 380$, two-dimensional nucleation also occurs on flat terraces. However, the nucleation process is still enhanced along monolayer step edges.

{001}. After injecting a $(Ba,Sr)SO_4$ solution with 30 µM $BaSO_4$ and 550 µM $SrSO_4$ into the AFM fluid cell, islands with a height of about 3.5 Å form (Fig. 7a). These islands do not cover the entire crystal surface, but rather their formation is restricted to a narrow area close to the rim along monolayer step edges parallel to <120>. Unfortunately, AFM does not provide information about the chemical composition of the precipitates. However, following Lippman's approach to describe solid solution aqueous systems (Lippmann, 1980; Glynn & Reardon, 1990), one can calculate a supersaturation function with respect to the $(Ba,Sr)SO_4$ solid solution. The given solution has the highest supersaturation (S = 171) with respect to an almost pure $BaSO_4$ endmember. It has been shown that two-dimensional nucleation in the $(Ba,Sr)SO_4$ system is consistent with Lippmann's thermodynamic approach (Pina et al., 1999). Therefore, it will be assumed that the islands shown in Fig 7a consist of a $BaSO_4$-rich phase. The fact that two-dimensional nucleation under the given conditions is restricted to monolayer step edges suggests that these sites are energetically favorable with respect to the formation of critical nuclei. The lattice mismatch between barite and celestite can be overcome by elastic deformation of the precipitating phase as well as the substrate (Walton, 1965). Considering the lattice parameters, the formation of two-dimensional barite nuclei on a celestite {001} substrate implies that the barite lattice is compressed, whereas the celestite lattice is expanded. Quantum mechanical calculations of stepped mineral surfaces (Vaughan et al., 1997) indicate that the atomic structure is relaxed in the vicinity of molecular steps. Therefore, small lattice mismatches between the precipitating phase and the substrate can be accommodated most easily near step edges. Similar nucleation behavior has been observed for various heterogeneous precipitation processes, such as the epitaxial formation of $NaNO_3$ on a $CaCO_3$ substrate (Chernov, 1984), or the precipitation of MnOOH onto an albite substrate (Junta-Rosso & Hochella, 1997). The reactive surface area for these heterogeneous reactions is only a small fraction of the entire crystal surface. In contrast, in the case of barite precipitation onto a barite {001} substrate, there are no preferred nucleation sites.

At a higher supersaturation of $S = 380$, two-dimensional nucleation also occurs on atomically flat terraces, however at a smaller rate compared to monolayer step edges (Fig. 7b). In addition to elastic deformation the lattice mismatch between precipitating barite and celestite substrate can also be overcome by the formation of dislocations at the interface. Apparently, this requires a higher degree of supersat-

uration and consequently a faster precipitation rate.

The supersaturation-dependent limits of the reactive surface area for two-dimensional nucleation in solid solution aqueous systems are an excellent example of crystal growth complexity in natural systems. At a supersaturation of $S = 171$ the reactive surface area depends on the step density. Under these conditions only about 2% of the total surface area was reactive with respect to the formation of two-dimensional nuclei. The reactive surface area increases with the degree of supersaturation. At $S = 380$ the entire crystal surface becomes reactive. Due to the variations in reactive surface area, macroscopically-derived growth rate laws under such conditions cannot easily be interpreted with respect to the dominant precipitation mechanism. Deriving surface area-normalized growth rates based on BET surface areas can vary significantly due to the nonlinear variation of the reactive surface area with changing degrees of supersaturation.

6. CONCLUSIONS

Macroscopically-derived crystal growth rates cannot be understood without microscopic information about the actual molecular scale growth mechanisms. However, fluid cell AFM observations open the possibility of obtaining details on monolayer step growth, spiral growth, and two-dimensional nucleation under controlled conditions and determining their intrinsic growth rate. In the case of barite, the contribution of these growth mechanisms to the overall growth rate changes with increasing degree of supersaturation. Monolayer step growth associated with cleavage steps and growth spirals is the predominant mechanism below a supersaturation of $40 < S < 50$. Above a supersaturation of $S > 40$-50, two-dimensional nucleation and the subsequent lateral spreading of islands contributes more than 50% to the total crystal growth rate. The intrinsic rate of $BaSO_4$ attachment to molecular steps changes with increasing supersaturation. In addition, the attachment of growth units does not involve the entire mineral surface since only a small fraction is reactive with respect to growth. The reactive surface area changes nonlinearly with the dominant growth mechanism and the degree of supersaturation. Fluid cell AFM experiments simultaneously provide quantitative information about the reaction rate at molecular scales and the reactive surface area. The macroscopic mineral growth rate is a function of both the intrinsic molecular scale attachment of growth units and the reactive surface area. Their complex relation can be unraveled by combining macroscopic growth experiments with microscopic AFM observations.

Acknowledgements—Many thanks are due to the Münster Mineral Surface group, which includes U. Becker, F. Brandt, C.M. Pina, A. Putnis, and P. Risthaus. The help of H. Pieper and V. Rapelius in the chemistry lab is also greatly appreciated. Financial support by the Deutsche Forschungsgemeinschaft is gratefully acknowledged. Constructive reviews by M. F. Hochella, Jr., G. Jordan, H. H. Teng, and an anonymous reviewer helped to improve the manuscript.

Editorial handling: Roland Hellmann

REFERENCES

Benton W. J., Collins I. R., Grimsey I. M., Parkinson G. M., and Rodger S. A. (1993) Nucleation, growth and inhibition of barium sulfate controlled modification with organic and inorganic additives. *Faraday Disc.* **95**, 281-297.

Blount C. W. (1977) Barite solubilities and thermodynamic quantities up to 300 °C and 1400 bars. *Am. Mineral.* **62**, 942-957.

Bosbach D., Hall C., and Putnis A. (1998) Mineral precipitation and dissolution in aqueous solution: in-situ microscopic observations on barite (001) with atomic force microscopy. *Chem. Geol.* **151**, 143-160.

Bosbach D., Charlet L., Bickmore B. R., and Hochella M. F. Jr. (2000) The dissolution of hectorite: An in-situ, real-time study using Atomic Force Microscopy. *Am. Mineral.* **85**, 1209-1216.

Brady P. V. and House W. A. (1996) Surface controlled dissolution and growth of minerals. In *Physics and Chemistry of Mineral Surfaces* (ed. P.V. Brady). CRC Press, New York. pp. 225-305.

Brown G. E., Parks G. A., and O´Day P. A. (1995) Sorption at mineral – water interfaces: macroscopic and microscopic perspectives. In *Mineral Surfaces* (eds. D.J. Vaughan & R.A.D. Pattrick). Chapman & Hall, London. pp. 129-184.

Burton W. K., Cabrera N., and Frank F. C. (1951) The growth of crystals and the equilibrium structure of their surfaces. *Philos. Trans. Royal Soc.* **A243**, 299-358.

Cathles L. M. (1983) An analysis of the hydrothermal system responsible for massive sulphide deposition in the Hokuroku Basin of Japan. *Econ. Geol. Monogr* **5**, 439-487.

Chernov A. A. (1984) *Modern Crystallography III. Crystal Growth*. Springer. Heidelberg.

Colville A. A. (1967) A refinement of the structure of barite. *Am. Mineral.* **52**, 1877-1880.

Deer W. A., Howie R. A., and Zussman J. (1992) *An Introduction to the Rock Forming Minerals.* Longman. Essex.

Doremus R. H. (1958) Precipitation kinetics of ionic salts from solution. *J. Phys. Chem.* **62**, 1068-1073.

Dove P. M. and Platt F. M. (1996) Compatible real-time rates of mineral dissolution by Atomic Force Microscopy (AFM). *Chem. Geol.* **127**, 331-338.

Glynn P. D. and Reardon E. J. (1990) Solid solution aqueous solution equilibria: thermodynamic theory and representation. *Am. J. Sci.* **290**, 164-201.

Hardy J. A. and Simm I. (1996) Low sulfate seawater mitigates barite scale. *Oil & Gas Journal* **94**, 64-67.

Hartman P. (1987) Modern PBC theory. In *Morphology of Crystals* (ed. I. Sunagawa). Terra Scientific Publishing Company. Tokyo. pp 209-253.

Hartman P. and Strom C. S. (1989) Structural morphology of

crystals with barite ($BaSO_4$) structure: A revision and extension. *J. Crystal Growth* **97**, 502-512.

Haul R. and Dümbgen G. (1960) Vereinfachte Methode zur Messung von Oberflächengrößen durch Gasadsorption. *Chem. Ing. Tech.* **32**, 349-354

He S., Oddo J. E., and Tomson M. B. (1995) The nucleation kinetics of barium sulfate in NaCl solutions up to 6 m and 90 °C. *J. Colloid Interface Sci.* **174**, 319-326.

Higgins S. R., Jordan G., Eggleston C. M., and Knauss K. G. (1998) Dissolution kinetics of the barium sulfate (001) surface by hydrothermal atomic force microscopy. *Langmuir* **14**, 4967-4971.

Hillig W. B. (1966) A derivation of classical two-dimensional nucleation kinetics and the associated crystal growth laws. *Acta Metallurgica* **14**, 1868-1869.

Hochella M. F. Jr. (1990) Atomic structure , microtopography, composition and reactivity of mineral surfaces. In *Mineral-Water Interface Geochemistry* (eds. M.F. Hochella and A.F. White). Reviews in Mineralogy **23**. Mineralogical Society of America, Washington D.C. pp. 87-132.

Johnson J. W., Knaus K. G., Glassley W. E., DeLoach L. D., and Tompson A. F. B. (1998) Reactive transport modeling of plug-flow reactor experiments: quartz and tuff dissolution at 240 °C. *Journal of Hydrology* **209**, 81-111.

Junta-Rosso J. L. and Hochella M. F. Jr. (1997) Linking microscopic and macroscopic data for heterogeneous reactions illustrated by the oxidation of manganese (II) at mineral surfaces. *Geochim. Cosmochim. Acta* **61**, 149-159.

Lasaga A. C. (1995) Fundamental approaches in describing mineral dissolution and precipitation rates. In *Chemical Weathering Rates of Silicate Minerals* (eds. A.F. White and S.L Brantley). Reviews in Mineralogy **31**. Mineralogical Society of America. Washington D.C. pp 23-86.

Lasaga A. C. (1998) *Kinetic Theory in the Earth Sciences*. Princeton University Press. Princeton.

Lefèvre F., Sardin M., and Schweich D. (1993) Migration of strontium in clayey and calcareous sandy soil: precipitation and ion exchange. *J. Contaminant Hydrology* **13** (1993) 215-229.

Lichtner P. C., Steefel C. I., and Oelkers E. H. (1996) *Reactive Transport in Porous Media*. Reviews in Mineralogy, Vol. 34, Mineralogical Society of America, Washington D.C.

Lippmann F. (1980) Phase diagrams depicting aqueous solubility of binary carbonate systems. *N. Jb. Mineral. Abh.* **139**, 1-25.

Liu S. T., Nancollas G. H., and Gasiecki E. A. (1976) Scanning electron microscopic and kinetic studies of the crystallization and dissolution of barium sulfate crystals. *J. Crystal Growth* **33**, 11-20.

Nielsen A. E. (1964) *Kinetics of Precipitation*. Pergamon Press, Oxford.

Nielsen A. E. (1984) Electrolyte crystal growth mechanisms. *J. Crystal Growth* **67**, 289-310.

Nielsen A. E. and Söhnel O. (1979) Interfacial tensions of electrolyte crystal – aqueous solutions from nucleation data. *J. Crystal Growth* **11**, 233-242.

O'Hara M. and Reid R. C. (1973) *Modeling Crystal Growth Rates from Solution*. Prentice-Hall, Englewood-Cliffs.

Park N. S., Kim M.-W., Langford S. C., and Dickinson J. T. (1996) Atomic layer wear of single crystal calcite in aqueous solution using scanning force microscopy. *J. Appl. Phys.* **80**, 2680-2686.

Parkhurst D. L. (1995) *User's guide to PHREEQC—a computer program for speciation, reaction-path, advective-transport, and inverse geochemical calculations*. U.S. Geological Survey Water-Resources Investigations Report 95-4227.

Paytan A., Moore W. S., and Kastner M. (1996) Sedimentation rate as determined by ^{226}Ra activity in marine barite. *Geochim. Cosmochim. Acta.* **60**, 4113-4319.

Pina C. M., Becker U., Risthaus P., Bosbach D., and Putnis A. (1998a) Molecular-scale mechanisms of crystal growth in barite. *Nature* **395**, 483-486.

Pina C. M., Bosbach D., Prieto M., and Putnis A. (1998b) Microtopography of the barite (001) face during growth: AFM observations and PBC theory. *J. Crystal Growth* **187**, 119-125.

Pina C. M., Enders M., and Putnis A. (1999) The composition of solid solutions crystallizing from aqueous solutions: the influence of supersaturation and growth mechanisms. *Chem. Geol.* **168**, 195-210.

Putnis A., Junta-Rosso J. L., and Hochella M. F. Jr. (1995) Dissolution of barite by a chelating agent: an atomic force microscopy study. *Geochim. Cosmochim Acta* **59**, 4623-4632.

Reardon E. J. and Armstrong D. K. (1987) Celestite ($SrSO_4$(s)) solubility in water, seawater and NaCl solution. *Geochim. Cosmochim. Acta* **51**, 942-957.

Rimstidt J. D. (1997) Gangue Mineral Transport and Deposition. In *Geochemistry of Hydrothermal Ore Deposits* (ed. H.L. Barnes). Wiley, New York..

Rufe E. and Hochella M. F. Jr. (1999) A quantitative assesment of reactive surface area in silicate dissolution. *Science* **285**, 874-876.

Steefel C. I. and Lasaga A. C. (1992) Putting transport in water-rock interaction models. *Geology* **20**, 680-684.

Stumm W. and Morgan J. J. (1995) *Aquatic Chemistry*. John Wiley, New York.

Sunagawa I. (1987) Surface microtopography of crystal faces. In *Morphology of Crystals* (ed. I. Sunagawa). Terra Scientific Publishing, Tokyo. pp 509-553.

Vaughan D. J., Becker U., and Wright K. (1997) Sulphide mineral surfaces: theory and experiment. *Int. J. Miner. Process.* **51**, 1-14.

Walton A. G. (1965) Nucleation of crystals from solution. *Science* **148**,601-607.

Zhang J.-W. and Nancollas G. H. (1990) Mechanisms of growth and dissolution of sparingly soluble salts. In *Mineral-Water Interface Geochemistry* (eds. M.F. Hochella, Jr. and A.F. White). Reviews in Mineralogy **23**, Mineralogical Society of America, Washington D.C. pp 365-396.